Inorganic Chemistry

pubs.acs.org/IC Article

Synthesis and Characterization of Pyrochlore-Type Praseodymium Stannate Nanoparticles: An Effective Electrocatalyst for Detection of Nitrofurazone Drug in Biological Samples

Ramachandran Rajakumaran, Ramaraj Sukanya, Shen Ming Chen,* Raj Karthik, Carmel B. Breslin, and P. Muhammed Shafi*

Cite This: *Inorg. Chem.* 2021, 60, 2464−2476 Read Online

ACCESS | Metrics & More | Article Recommendations | Supporting Information

ABSTRACT: Apart from perovskites, the development of different types of pyrochlore oxides is highly focused on various electrochemical applications in recent times. Based on this, we have synthesized pyrochlore-type praseodymium stannate nanoparticles ($Pr_2Sn_2O_7$ NPs) by using a coprecipitation method and further investigated by different analytical and spectroscopic techniques such as X-ray diffraction, Raman spectroscopy, field emission-scanning electron microscopy, high resolution-transmission electron microscopy, and X-ray photoelectron spectroscopy analysis. Followed by this, we have designed a unique and novel electrochemical sensor for nitrofurazone detection, by modifying the glassy carbon electrode (GCE) with the prepared $Pr_2Sn_2O_7$ NPs. For that, the electrochemical experiments were performed by using cyclic voltammetry and differential pulse voltammetry techniques. The $Pr_2Sn_2O_7$ NPs modified GCE exhibits high sensitivity (2.11 $\mu A\ \mu M^{-1}\ cm^{-2}$), selectivity, dynamic linear ranges (0.01−24 μM and 32−332 μM), and lower detection limit (4 nM). Furthermore, the $Pr_2Sn_2O_7$ NPs demonstrated promising real sample analysis with good recovery results in biological samples (human urine and blood serum) which showed better results than the noble metal catalysts. Based on these results, the present work gives clear evidence that the pyrochlore oxides are highly suitable electrode materials for performing outstanding catalytic activity toward electrochemical sensors.

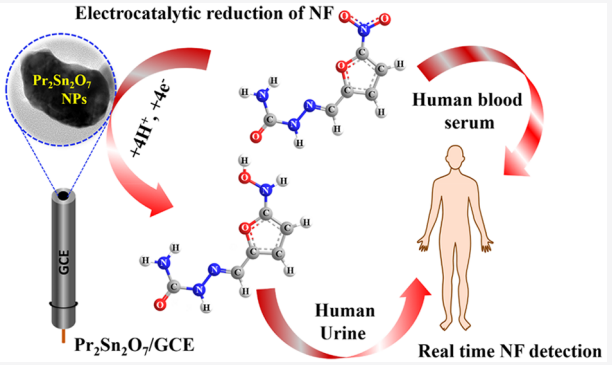

INTRODUCTION

Metal oxide-based electrocatalysts, particularly pyrochlore oxides and perovskite, have been broadly considered as dual-functional catalysts in various electrochemical applications, namely, oxygen evolution reaction (OER), batteries, solid oxide fuel cells, oxygen reduction reaction (ORR), and electrochemical sensors.[1−8] In that classification, there have been substantial efforts devoted to the study of various transition metal oxide nanostructures including rutile, spinel, perovskite, rock salt, and bixbyite.[9] Moreover, a brief summary of the history, defect chemistry, and transport properties of perovskite oxides (PV oxides) has been already discussed and documented clearly.[10] Apart from PV oxides, ceramic-like pyrochlore oxides with the formula of $A_2B_2O_7$ are a well-known family that serves as an assuring inorganic material and acts as a typical catalyst in electrochemical studies. Moreover, these pyrochlores explore a wide range of essential ions and this superior group holds fascinating properties such as good thermal conductivity, geometrically frustrated magnetism, earth element waste storage capacity, electrical, and ionic conductivity that can be efficiently delimited by altering the elemental ions.[11−17] In general, pyrochlore oxides are a classic type of ceramic materials with the general formulation of $A_2B_2O_6O$ or $A_2B_2O_7$, where A (A = Tb, Eu, Sm, Gd, and Ce) and B (B = Sn, Zr, Ti, or Zr) are the trivalent and tetravalent cations, respectively, and comprise a huge set of inorganic compounds.[18] In that, there are two types of oxygen composition such as $(A_2B_2O_6O)$ or $[A_2O]$ $[B_2O_6]$ containing A and O atoms existing with interstitial sites (A_2O) and coordinated by a network of corner-sharing BO_6 octahedra groups. Thus, the oxygen ions on the 48f site (2-O48f) are surrounded by two A and two B cations and the oxygen ions on the 8b sites (2-O8b) are surrounded by four A cations. These large A-ions are bonded to eight oxygen ions and occupy the 16d site. In addition to that, the small B-ions are coordinated to six oxygen ions forming a trigonal antiprism by filling in the 16c site.[18,19] In addition, the crystalline structure and stability of pyrochlores are mainly related to the composition and ratio of radii of the A-site cation (rA^{3+}) and B-site cation (rB^{4+}) or the

Received: November 15, 2020
Published: February 3, 2021

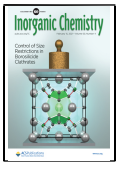

https://dx.doi.org/10.1021/acs.inorgchem.0c03377
Inorg. Chem. 2021, 60, 2464−2476

oxygen vacancies. Based on the oxygen vacancies, the pyrochlore structure closely resembles the uniformly arranged inadequate fluorite structure (space group $Fd\bar{3}m$). Due to the combination of aforementioned crystal structures, the pyrochlore oxides such as $Y_2Ti_2O_7$, $Eu_2Ti_2O_7$, $Y_2Ru_2O_7$, and $Nd_2Sn_2O_7$ have been successfully synthesized and utilized as electrocatalyst for various electrochemical applications because of their tunable lattice structure, high chemical stability, and the existence of abundant oxygen vacancies.[4,19−22] In addition to that, the ability to substitute different ions into the A- and B-site elements while maintaining the same crystal structure provides another powerful strategy to tune the concentration of oxygen vacancies, electronic structures, and their electrochemical activity.[5]

The rare-earth (RE) pyrochlore stannate compounds ($M_2Sn_2O_7$, M = rare-earth ions (La, Y, Dy, and Pr)) are recently focused as an ecofriendly catalyst because of their structural order, abundant surface oxygen sites, and admirable stability when compared to other PV oxides.[23] Particularly, these geometrically frustrated pyrochlores are well-known to show a complex spin−orbital coupling phenomenon which is highly responsible for metals and host or analyte molecule interaction during electrochemical reactions. Based on this aspect, a few types of rare-earth or lanthanide stannates (LSO) such as $La_2Sn_2O_7$, $Dy_2Sn_2O_7$, and $Nd_2Sn_2O_7$ are widely used as an electrocatalyst for various applications including photocatalysis, electrochemical conversion, and storage because of their significant properties in terms of high surface area, fast charge transferability, high melting point, lower activation energy, eminent chemical stability, and ionic mobility.[22−25] It is observed that there is a strong conflict between the accelerated covalent interactions in the continuous filling of 4f orbital which results in the enhancement of ionicity and higher electronegativity among rare-earth oxides (RE-O). Among these lanthanide stannate series, praseodymium stannate ($Pr_2Sn_2O_7$-PSO) is a highly trending material in electrochemical studies, due to their unique crystal structure and high spin−orbital coupling interaction.[26] In addition to that, this coupling effect relates to the strong quantum confinement (phonon interaction) accompanied by a change in heterogeneous spin-state, and may lead to the occurrence of unbalanced Coulombic charge. It enables the formation of a large number of surplus active sites and the enhancement of catalytic activity. For example, Abraham et al. explained the electrochemical properties of PSO based on doping heterogeneous compounds (defect chemistry).[26] In PSO, Pr^{3+} (8-coordination of the ideal cube structure) shows the large ionic size (Pr ion: 112.6 pm) and small moment, followed by interaction with Sn^{4+} (6-coordinated distorted octahedral coordination), which will lead to the creation of more electronic charges, thereby improving the electron transfer path for the electrochemical reactions.[26] Based on these concepts, we believe that the $Pr_2Sn_2O_7$ pyrochlore oxide is a suitable candidate for electrochemical sensing of target molecules.

Nitrofurazone (5-nitro-2-furfural semicarbazone, NF) is derived from the nitrofuran family of antibiotics. It is highly reactive against various types of Gram-positive and Gram-negative bacteria and broadly used to treat bacterial diseases produced by *Escherichia coli*, *Salmonella* species, and several protozoan infections (e.g., trypanosomiasis).[27,28] Further, it can be employed to treat skin infections and trypanosomiasis.[29,30] NF is capable of inducing carcinogenic and teratogenic behavior, and it is widely consumed by humans via the food chain.[27] In additon, NF is used as a feed additive among farm animals and aquatic species to increase productivity and is mainly used for healing of burns. The prolonged consumption of NF causes chronic toxicity giving rise to the side effects of hemolytic anemia and thrombocytopenia. Due to these reasons, the Chinese Ministry of Agriculture (CMA) and the European Union (EU) has strictly banned the usage of NF for humans and animals.[31,32] Furthermore, NF possesses high antimicrobial properties and is cost-effective, and hence, it is still illegally used to a substantial level in humans and farm animals. Therefore, it is essential to develop and monitor NF with a rapid, sensitive analytical technique affording the detection of NF concentration. Different types of traditional analytical techniques have been established including high-performance liquid chromatography−mass spectrometry (HPLC-MS), paper chromatography and spectrophotometry, and so on for the detection of NF.[33−35] On comparing with the above-mentioned analytical methods, the voltammetry techniques are highly preferred due to convenient portability, easy sample preparation and processing, massive sensitivity, and quick detection time. To perform the electrochemical sensing process, the choice of highly active electrode material is mandatory for the modification of the electrode surface. As because of the unique electrochemical nature of PSO, we believe that this pyrochlore oxide is a highly suitable active electrode material toward the detection of NF.

In this work, we have synthesized praseodymium stannate nanoparticles ($Pr_2Sn_2O_7$ NPs) by a feasible coprecipitation approach. The as-prepared $Pr_2Sn_2O_7$ NPs were investigated by numerous analytical techniques such as XRD, Raman, and XPS analysis. The surface morphology was examined by using FE-SEM, and HR-TEM analysis. The as-prepared $Pr_2Sn_2O_7$ NPs drop casted GCE was used for the electrochemical determination studies. From the electrochemical studies, it is clear that the $Pr_2Sn_2O_7$ NPs/GCE shows higher electrocatalytic activity with a lower limit of detection (LOD) and eminent sensitivity toward sensing of NF. Further, the prepared $Pr_2Sn_2O_7$/GCE was used for the recovery analysis test with the help of human urine and blood serum samples. Hence, we hope that the $Pr_2Sn_2O_7$ NPs are potential material for the detection of NF in biological and pharmaceutical applications.

EXPERIMENTAL SECTION

Materials and Reagents. Praseodymium nitrate hexahydrate ($Pr(NO_3)_3.6H_2O$, 99.9%), urea, sodium stannate trihydrate ($Na_2SnO_3.3H_2O$, 95%), sodium phosphate monobasic dihydrate ($NaH_2PO_4.2H_2O$, ≥99.0%), sodium phosphate dibasic anhydrous (Na_2HPO_4, 99%), and nitrofurazone (NF, ≥97.0%) were obtained from Sigma-Aldrich, Taiwan. The above chemicals were used directly for the experimental process without any other treatment and purification process. For performing the electrochemical test, the required electrolyte (phosphate buffer solution (0.05 M PBS)) was prepared by intermixing both phosphate precursors. For preparing the different pH solutions, the pH was adjusted by using hydrochloric acid (HCl) and sodium hydroxide (NaOHn). Double distilled water (DD) was used for preparing the necessary solution, which is mandatory for the electrochemical studies.

Preparation of Rare-Earth Pyrochlore Praseodymium Stannate. The RE pyrochlore $Pr_2Sn_2O_7$ NPs were prepared by a cost-effective coprecipitation method. The required precursors for the synthesis of $Pr_2Sn_2O_7$ are $Pr(NO_3)_3{\cdot}6H_2O$, $Na_2SnO_3{\cdot}3H_2O$, and urea. Initially, 0.2 M $Pr(NO_3)_3.6H_2O$ was dissolved in 35 mL of DD water under magnetic stirring for 20 min to obtain a transparent green colored ionic solution. Followed by this, urea of about 5 g/10 mL and 0.4 M $Na_2SnO_3{\cdot}3H_2O$ in 35 mL of DD water solutions were prepared and slowly added to the above ionic solution to obtain the light green colored precipitate. Then the homogeneous precipitated mixture

https://dx.doi.org/10.1021/acs.inorgchem.0c03377
Inorg. Chem. 2021, 60, 2464−2476

Scheme 1. Coprecipitation Preparation of RE Pyrochlore $Pr_2Sn_2O_7$ NPs

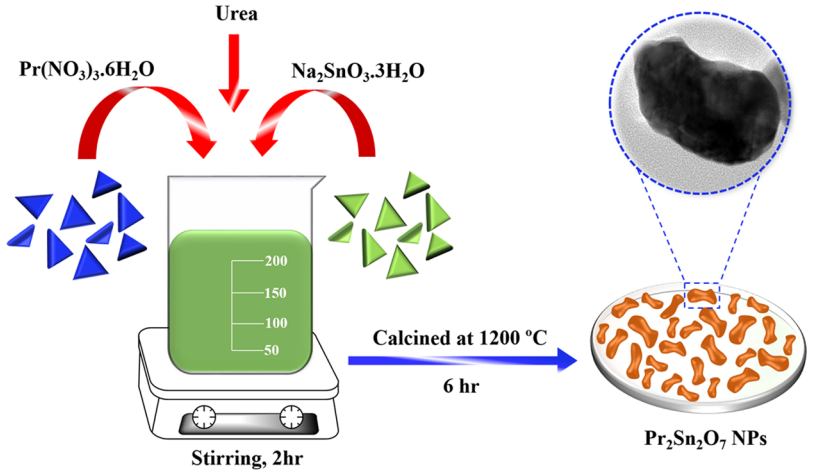

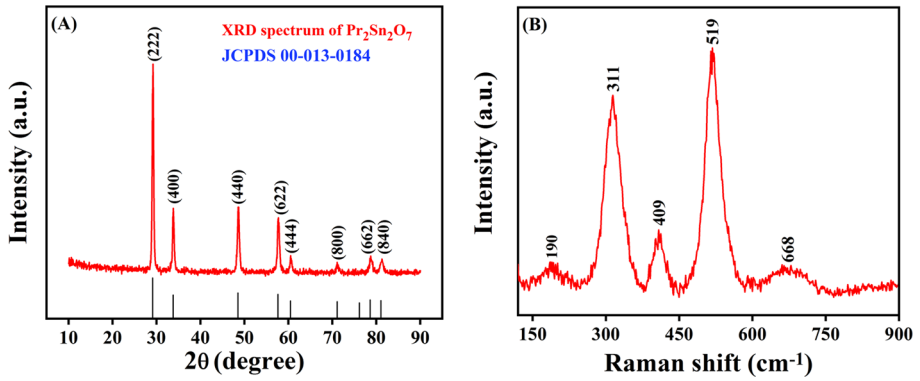

Figure 1. (A) X-ray diffraction patterns and (B) Raman spectra of $Pr_2Sn_2O_7$ NPs.

solution was constantly stirred for 2 h. After that, the obtained turbidity solution mixture was vigorously centrifuged for 20 min at 5000 rpm. The centrifugation process was repeated four to five times, and the obtained precipitate was washed several times in water followed by the use of ethanol. The supernatant solution was washed out, and the obtained precipitate was dehydrated in a vacuum oven. Finally, the acquired light green colored powder was calcined under the air atmosphere at a temperature of 1200 °C for 6 h. After the completion of the calcination process, the light green color was changed into a light brown color powder. The coprecipitation synthesis procedure for RE pyrochlore $Pr_2Sn_2O_7$ NPs is illustrated in Scheme 1. The obtained product of $Pr_2Sn_2O_7$ NPs was further utilized for the characterization and electrochemical studies.

Characterization Techniques. The as-prepared $Pr_2Sn_2O_7$ NPs were initially examined to determine the phase purity formation and confirmed by X-ray diffraction analysis (XRD, PANalytical X'Pert PRO diffractometer with the source of Cu Kα radiation (K = 1.541 Å)). Then the crystallographic patterns were obtained over the diffraction scanning range (scan rate: 10° per minute) from 10 to 90°. The polarizability and the molecular vibrations of the as-prepared $Pr_2Sn_2O_7$ NPs were obtained by Raman spectroscopy (Dongwoo Ramboss 500i Micro-Raman/PL spectrometer system with a 532 nm laser). The comprehensive textural morphology, lattice distortion, and elemental composition were investigated by field emission scanning electron microscopy (FE-SEM, ZEISS Sigma 300 microscope), energy-dispersive X-ray spectroscopy (EDS), and high resolution-transmission electron microscopic analysis (HR-TEM; Shimadzu JEM 1200 EX-STEM). Furthermore, the surface analysis of the prepared $Pr_2Sn_2O_7$ NPs was carried out by X-ray photoelectron spectroscopy (XPS, Thermo scientific multilab 2000) technique.

Electrode Construction and Electrochemical Measurements. Initially, the GCE (3 mm diameter, working area = 0.07 cm^2) was cleaned carefully with aqueous alumina slurry (0.05 μm) and completely washed with copious amounts of water followed by ethanol to attain a clean surface. Meanwhile, the as-prepared $Pr_2Sn_2O_7$ NPs were weighed to give a concentration of 5 mg/mL and ultrasonicated for 20 min in a bath-sonicator to obtain a uniform suspension. Consequently, 6 μL of $Pr_2Sn_2O_7$ NPs aliquot was carefully drop casted on the surface of polished GCE. The $Pr_2Sn_2O_7$ NPs modified GCE was allowed to dry in a hot air oven for 10 min and further used for electrochemical investigations.

The complete electrochemical studies and analyses were performed by using electrochemical workstations (CH Instruments, Inc., USA), namely, differential pulse voltammetry (DPV, CHI 900) and cyclic voltammetry (CV, CHI 1205C). The entire electrochemical investigations were carried out by standard three-electrode edifice configuration using modified $Pr_2Sn_2O_7$/GCE as an operational electrode, platinum wire as a counter electrode, and Ag/AgCl (saturated KCl) served as a reference electrode. For the electrochemical detection of NF, the CV and DPV techniques were employed over the vast potential ranges from +0.4 to −0.8 V. Intending to drive out the influence of diffused oxygen present in PBS, all solutions were deoxygenated by purging with high purity (99.99%) nitrogen (N_2) flow for several minutes before performing each electrochemical measurement.

RESULTS AND DISCUSSION

The physical characteristic and geometrical nature of pyrochlore oxide- $Pr_2Sn_2O_7$ NPs was investigated using numerous analytical, spectroscopic techniques and the obtained results are systematically discussed in the section below.

In general, the crystallinity and phase purity nature of the as-prepared pyrochlore-$Pr_2Sn_2O_7$ NPs were evaluated by XRD

https://dx.doi.org/10.1021/acs.inorgchem.0c03377
Inorg. Chem. 2021, 60, 2464−2476

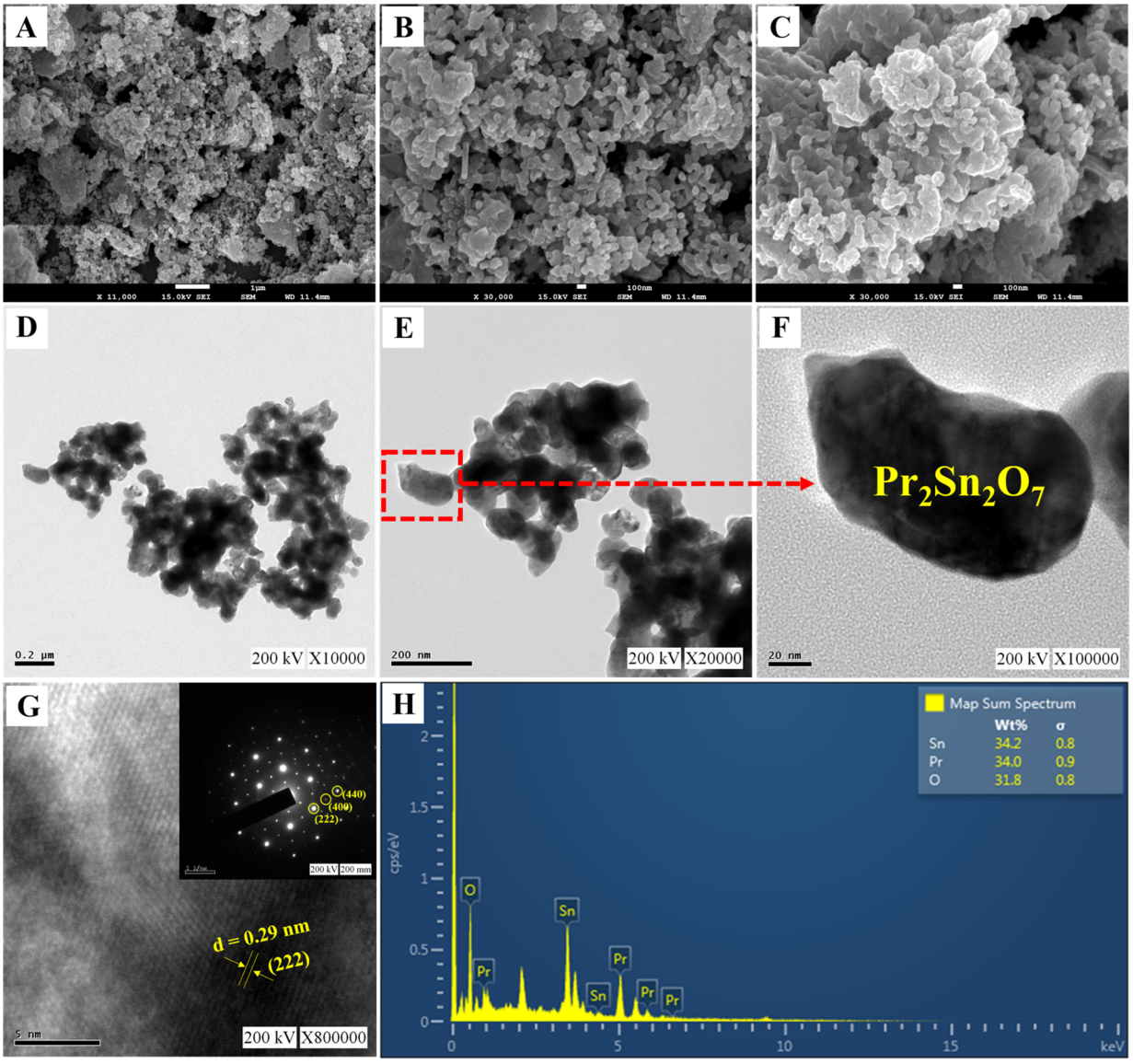

Figure 2. (A–C) FE-SEM and (D–G) HR-TEM images of $Pr_2Sn_2O_7$, (F) high magnification image, (G) lattice fringes (SAED-inset), and (H) EDS analysis of $Pr_2Sn_2O_7$.

analysis. The obtained typical diffraction patterns of the $Pr_2Sn_2O_7$ NPs sample is displayed in Figure 1A. Figure 1A shows clear distinctive diffraction peaks at 29.16°, 33.79°, 48.65°, 57.63°, 60.41°, 71.03°, 78.61°, and 81.09° corresponding to the (222), (400), (440), (622), (444), (800), (662), and (840) *hkl* planes of cubic lattice, respectively. The XRD peaks are indexed to pyrochlore-$Pr_2Sn_2O_7$ NPs with the cubic lattice and lattice constant of a = 1.06 nm, which is well-concordant with the standard card [JCPDS 00-013-0184]. The impurity peaks of components like $Pr(OH)_3$ and SnO_2 were not observed, revealing the solid and pure crystalline nature of pyrochlore-type oxide such as $Pr_2Sn_2O_7$ NPs. This XRD result suggests that the crystalline $Pr_2Sn_2O_7$ NPs was prepared by a simple coprecipitation synthesis at an adequately low temperature. Along with that, the average particle size of the prepared $Pr_2Sn_2O_7$ NPs sample was determined by employing the Debye–Scherrer eq 1:

$$D = k\lambda/\beta \cos\theta \quad (1)$$

where λ is the wavelength, D is the grain size of the particle, k is 0.9, and β is the full-width half-maximum. The average crystalline size of the pyrochlore-$Pr_2Sn_2O_7$ NPs was determined to be 4.65 nm. Further, the formation of pyrochlore oxide was confirmed by Raman analysis. The Raman spectroscopy gives detailed evidence and it is complementary to the XRD findings.

In general, the pyrochlore oxides (asymmetrical $A_2B_2O_7$) fall into two length scale classifications such as orthorhombic, which comes under a local scale of about less than 10 Å, and cubic, with a wide-range scale of periodicity. To explore the structure of the as-prepared sample, the Raman spectra of $Pr_2Sn_2O_7$ NPs are recorded in the range of 100–800 cm^{-1} as represented in Figure 1B. Moreover, it is well discussed in the previous literature that the ideal pyrochlore structured oxide shows six active Raman modes corresponding to (A–O) as well as (B–O) vibrational bonds, which is described by factor group analysis,[36] and is given below

$$G_{(Raman)} = A_{1g} + E_g + 4F_{2g} \quad (2)$$

https://dx.doi.org/10.1021/acs.inorgchem.0c03377
Inorg. Chem. 2021, 60, 2464–2476

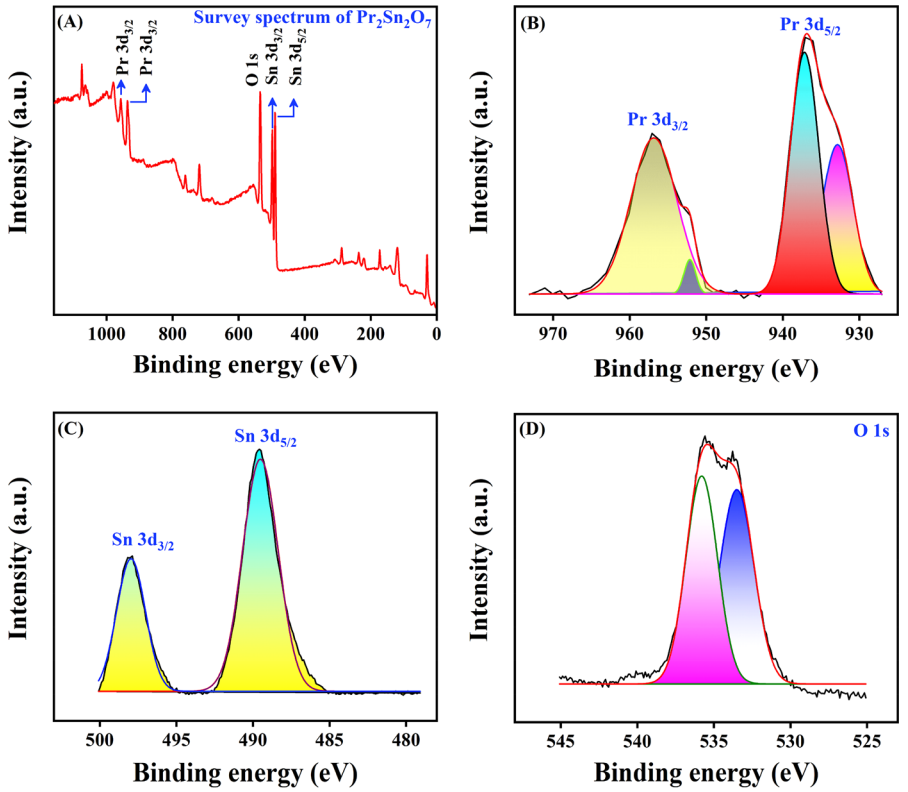

Figure 3. (A) Wide scan XPS spectra of $Pr_2Sn_2O_7$ NPs. High-magnification XPS spectra of (B) Pr 3d, (C) Sn 3d, and (D) O 1s.

Here, the F_{2g} mode is ascribed to the A−O and B−O bond stretching vibrations with bending vibrations, the A_{1g} mode corresponds to the O−B−O bending vibrations, and the E_g mode represents the B−O_6 bending vibrations. The Raman signal at 190 cm^{-1} belongs to the lattice soft modes, which is related to Sn−O bending vibration modes.[37] Followed by this, the peak observed around 311 cm^{-1} corresponds to the E_g mode and it is analogous to the corresponding O−Sn−O bond (Sn−O_6-bending vibration or Pr−O stretching).[38] Further, the peak at 409 cm^{-1} is attributed to the A_{1g} mode corresponding to the SnO_6 (torsional mode),[38] and the well-resolved peak at 519 cm^{-1} is coupled to the Sn−O stretching.[39] The Raman bands at 668 cm^{-1} were assigned to the F_{2g} modes and it occurs with the overlap of Sn−O bending and vibrational stretching caused by the Pr−O bonds.[40] The introduction of dynamic spin interaction (M/N) into the crystal lattice is clearly confirmed by the obtained Raman results. The M−O symmetrical stretching vibration exists with the unique vibrational modes; *i.e.*, the pyrochlore consists of a distorted octahedron, in which the six anions are typically coordinated to the Sn-site. Furthermore, the vacant 8b sites are tetrahedrally coordinated to the Sn-site cations of the 48f oxygen atoms. Besides, the octahedral "breathing" mode was assumed in stannates structure as that of other pyrochlore oxides. In addition to that, the observed intensities of the Raman peaks of $Pr_2Sn_2O_7$ samples are broadened and weakened, because of their disordered structure, and it influences the electrocatalytic activity of the as-prepared $Pr_2Sn_2O_7$ NPs.

Following this, morphologies of the pyrochlore oxide such as $Pr_2Sn_2O_7$ were observed by FE-SEM and HR-TEM, and the obtained results are displayed in Figure 2A−G. The FE-SEM images, at various magnifications, as in Figure 2A−C, suggest that the prepared $Pr_2Sn_2O_7$ sample is an ordered group of RE pyrochlore structures with a diameter around ∼100 nm. No other morphologies could be detected, indicating a high yield of this type of pyrochlore as in the form of nanoparticles. The $Pr_2Sn_2O_7$ NPs arrangement was arbitrarily agglomerated and did not have a close-packed system. Further, a detailed structural analysis of $Pr_2Sn_2O_7$ NPs was clearly investigated by using HR-TEM analysis. Figure 2D−F represents HR-TEM images of $Pr_2Sn_2O_7$ NPs and it is proved that the $Pr_2Sn_2O_7$ NPs exist with a single particle size of around ∼100 nm. In addition to that, the typical enlarged lattice HR-TEM image (Figure 2G) of $Pr_2Sn_2O_7$ carnivals the well-resolved lattice fringes for as-prepared pyrochlore-$Pr_2Sn_2O_7$ with the interplanar spacing distance of about 0.29 nm, which matches with XRD plane of (222) cubic pyrochlore oxide such as $Pr_2Sn_2O_7$. As displayed in Figure 2G, there is a large number of surface defects observed in the lattice plane. In the pyrochlore $Pr_2Sn_2O_7$ NPs, some of the lattice fringes are distorted and blurred; this mainly arises from the deficiency of oxygen atoms. The selected area electron diffraction (SAED) pattern of $Pr_2Sn_2O_7$ NPs is clearly observed with the corresponding bright rings (Figure 2G inset), and it can be well indexed to diffraction from the (222), (440), and (400) planes of cubic RE pyrochlore-type $Pr_2Sn_2O_7$, that illustrates the pure crystalline property architect nature of the particles. Along with that, the elemental composition of pyrochlore-type $Pr_2Sn_2O_7$ was probed by mapping analysis in FE-SEM, and the obtained mapping results are indicated in Figure S1. Figure S1B−D outlines the elements such as (34%) praseodymium (Pr, Figure S1B), (34.2%) tin (Sn, Figure S1C), and (31.8%) oxygen (O, Figure S1D). All elements are uniformly distributed on the as-prepared $Pr_2Sn_2O_7$ NPs without any other impurities, which suggests that the pyrochlore-type oxides can be formed by a simple synthesis method, in good agreement with the EDS results as displayed in Figure 2H. All morphological analyses

https://dx.doi.org/10.1021/acs.inorgchem.0c03377
Inorg. Chem. 2021, 60, 2464−2476

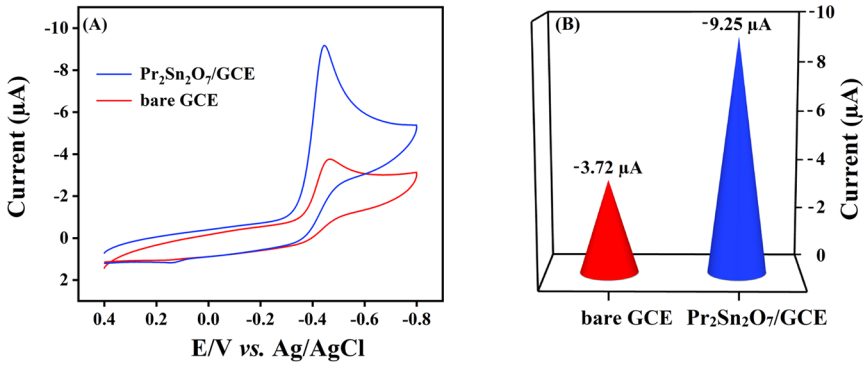

Figure 4. (A) Cyclic voltammogram response of bare GCE and $Pr_2Sn_2O_7$/GCE for 50 μM NF at a sweep rate of 50 mV/s at pH 7.0. (B) Bar diagram of different electrodes versus NF cathodic current.

Scheme 2. Feasible Mechanism for the NF Electrocatalytic Reduction at $Pr_2Sn_2O_7$/GCE

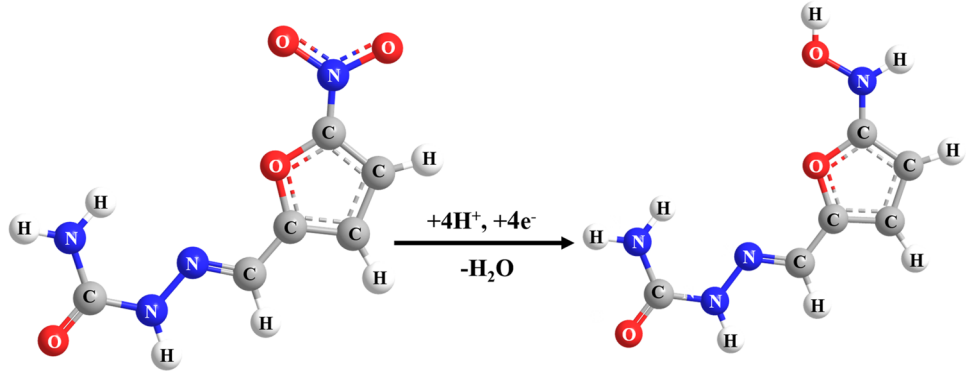

proved that the as-prepared $Pr_2Sn_2O_7$ particle size is in the nanometer range.

In general, the electrochemical behavior of $A_2B_2O_7$ pyrochlore catalysts is greatly affected because of the deficiency in surface oxygen atoms and valence state at the B-site. The core physicochemical surface properties and the chemical compositions of $Pr_2Sn_2O_7$ NPs were investigated by XPS analysis. Figure 3A represents the wide scan XPS spectrum, which shows the presence of all elements in the as-prepared pyrochlore $Pr_2Sn_2O_7$ NPs, namely, Pr 3d, Sn 3d, and O 1s, corresponding to the binding energies at 956.82, 498.01, and 535.77 eV, respectively. In addition to that, the high-magnified XPS spectra of Pr 3d, Sn 3d, and O 1s are represented in Figure 3B–D. Figure 3B shows the high-magnified spectrum of Pr deconvoluted with the respective binding energies at 936.92 and 956.82 eV, indicating the presence of Pr^{3+}, such as Pr $3d_{5/2}$ and Pr $3d_{3/2}$, correspondingly.[41] Consistently, the high-magnified spectra of Sn 3d (Figure 3C) exhibit a peak at 489.61 and 498.01 eV attributed to the ionic state of Sn^{4+} such as Sn $3d_{5/2}$ and Sn $3d_{3/2}$.[42] The O 1s spectra (Figure 3D) give well-defined peaks with the binding energies at 533.50 and 535.77 eV corresponding to the coordination of metal–oxygen bonds (Sn–O and Pr–O). In addition , the O 1s spectra indicate the presence of two different oxygen species on the surface. From the obtained curve, the XPS peak at 533.50 eV can be attributed to the oxygen lattice site. In addition to that, the O 1s peak was deconvoluted at a binding energy of 535.77 eV; it confirms the loosely bound oxygen species on the surface.[42] The acquired XPS results are in good agreement with those in previously reported articles. Based on the literature review, the relative percentage of oxygen in the surface determines the quantity of oxygen vacancies. As per discussion, the presence of oxygen vacancies or oxygen transport media will enable the essential electrocatalytic performance toward the sensing phenomenon. Furthermore, the imperfection in oxygen atoms is advantageous for the excellent migration of atoms and molecules during the electrochemical reaction.

Electrochemical Studies. *Electrochemical Reduction of NF at $Pr_2Sn_2O_7$/GCE.* The electrochemical sensing capability of $Pr_2Sn_2O_7$ NPs constructed GCE toward NF was investigated by using the CV technique, and the obtained results are displayed in Figure 4A. The electrochemical experiment was conducted in the electrochemical cell (pH 7.0) containing 50 μM NF under a N_2-saturated atmosphere at a sweep rate of 50 mV/s. The cathodic amplified NF signal for bare GCE and $Pr_2Sn_2O_7$/GCE is clearly observed in Figure 4A. For bare GCE, it shows only a low cathodic current response of −3.72 μA at −0.47 V, because of strong hindrance along with inferior electron transferability of bare GCE. Attractively, the $Pr_2Sn_2O_7$ NPs modified GCE delivers a well-defined and sharp cathodic peak current magnitude (I_{pc}) of −9.25 μA with a lower negative potential (E_{pc}) shift at −0.43 V, due to the higher active surface sites with superior electron transfer mobility. The obtained cathodic peak at −0.43 V corresponds to the irreversible reduction reaction of the nitro ($-NO_2$) group to the hydroxylamine group (−NHOH) with a four-electron ($4e^-$) and four-proton ($4H^+$) transfer process with the elimination of water molecules.[43−46] During the reverse scan, a small oxidation peak was observed at both modified and unmodified electrodes at the potential of around +0.14 V, which were related to the reversible oxidation

https://dx.doi.org/10.1021/acs.inorgchem.0c03377
Inorg. Chem. 2021, 60, 2464−2476

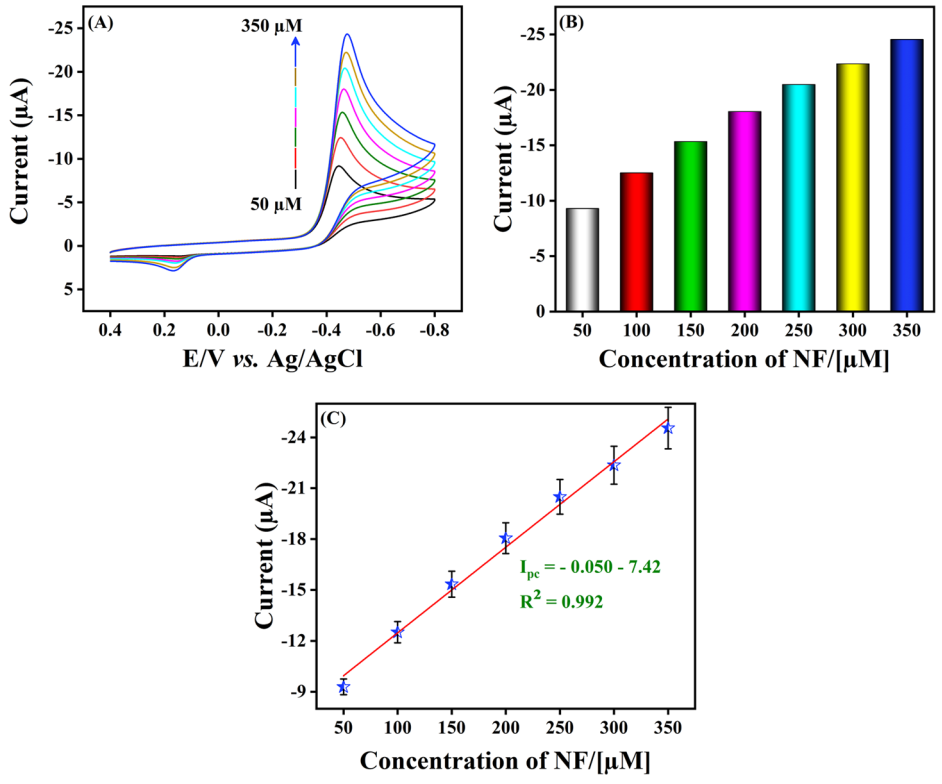

Figure 5. (A) Obtained CVs signals for various concentrations of NF from 50 to 350 μM at $Pr_2Sn_2O_7$/GCE. (B) Bar diagram for concentration versus NF reduction. (C) Linear plot for the NF concentration versus cathodic peak current.

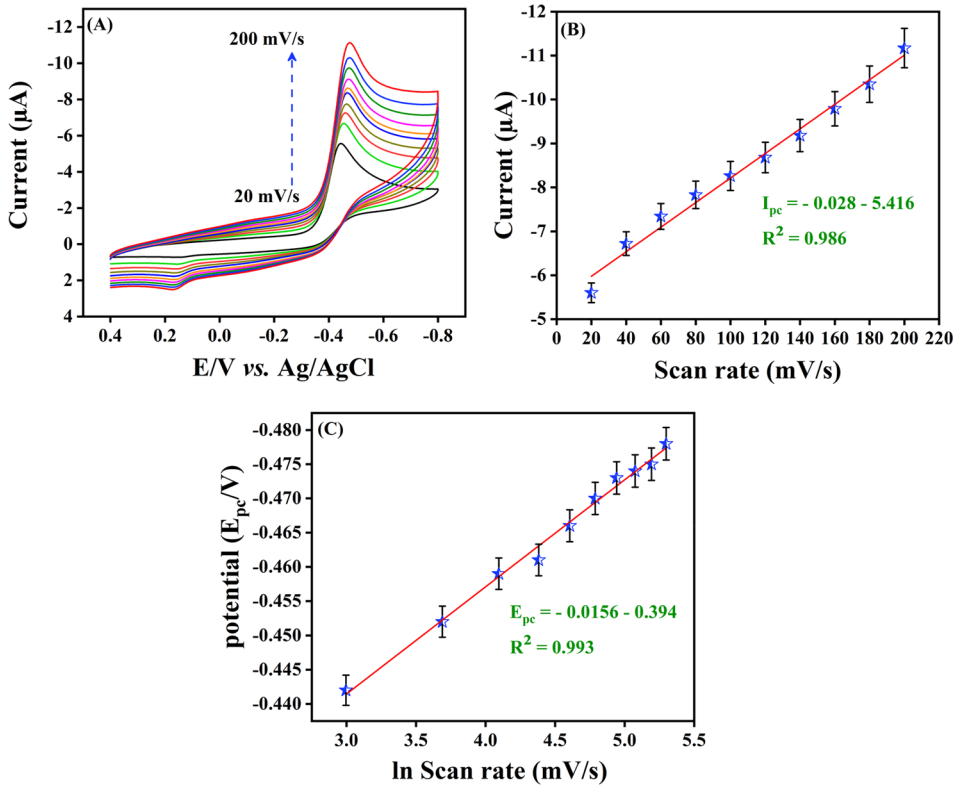

Figure 6. (A) CV curves for various scan rates from 20 to 200 mV/s in the presence of 50 μM NF in pH 7.0 at $Pr_2Sn_2O_7$/GCE. (B) Calibration plot for the scan rate (υ) versus NF cathodic current signal. (C) Linear plot of ln sweep rate versus cathodic peak potential (E_{pc}/V).

peak of −NHOH to nitroso derivatives with a two-electron ($2e^-$) and two-proton ($2H^+$) transfer process. The viable mechanism for the electrocatalytic NF reduction prevailing at $Pr_2Sn_2O_7$/GCE is outlined in Scheme 2. The acquired results propose that the enhanced catalytic activity of $Pr_2Sn_2O_7$ NPs is because of the greater interaction of NF and more active sites of

https://dx.doi.org/10.1021/acs.inorgchem.0c03377
Inorg. Chem. 2021, 60, 2464−2476

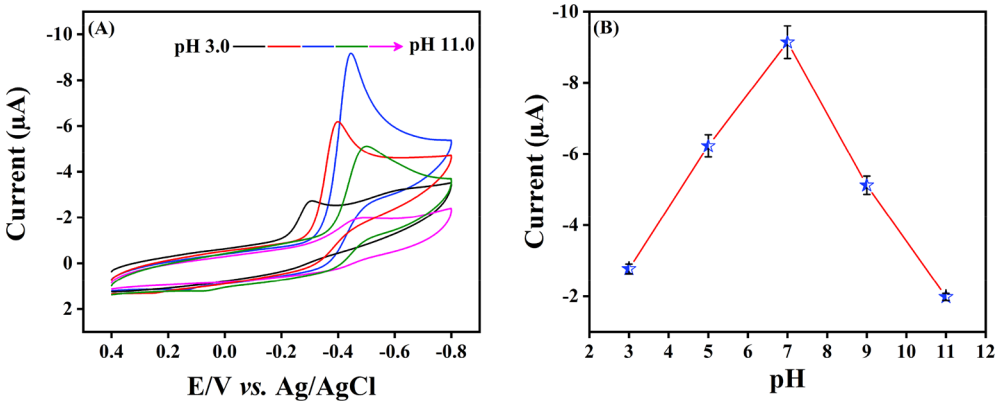

Figure 7. (A) CV curves for 50 μM at $Pr_2Sn_2O_7$/GCE at various pH values (pH 3.0, 5.0, 7.0, 9.0, 11.0) under a N_2-saturated atmosphere at a scan rate of 50 mV/s. (B) Linear plot for pH versus NF current signal.

the $Pr_2Sn_2O_7$ NPs, and it might offer a tremendous electrochemical sensing platform for NF detection. Moreover, the prepared $Pr_2Sn_2O_7$/GCE possesses 2.49-times higher current intensity than the bare GCE (Figure 4B) for the detection of NF.

Influence of Catalyst Loading on the GCE. Initially, 5 mg of the as-prepared catalyst was taken, dispersed in 1 mL of DD water, and ultrasonicated for 20 min to obtain a homogeneous suspension. The electrocatalytic activity of the as-prepared $Pr_2Sn_2O_7$ NPs toward the sensing of NF (50 μM) was investigated by loading different volumes of catalyst on the GCE surface, namely, 4, 6, 8, and 10 μL. The CV studies were carried out at pH 7.0 under N_2 atmosphere at a sweep rate of 50 mV/s, and the obtained CV current responses are shown in Figure S2A. It is obviously seen that the NF cathodic current signal accelerated from 4 to 6 μL loading of the catalyst ($Pr_2Sn_2O_7$) and gradually decreased from 8 to 10 μL. On moving toward a higher volume of the catalyst, loading may lead to agglomeration of the nanoparticles on the GCE surface and, simultaneously, the mobility of the electron was hindered toward NF reduction. Along with that, 6 μL of the catalyst loading exhibits a higher cathodic current response with lower potential shift when compared to 4, 8, and 10 μL. From these findings, we have selected 6 μL of the prepared suspension as an optimal catalyst loading amount for further electrochemical studies. The corresponding bar diagram for the catalyst loading and the obtained NF CV signals were displayed in Figure S2B.

Influence of Concentration. To analyze the NF quantitative reduction as well as the electrocatalytic activity of the constructed $Pr_2Sn_2O_7$/GCE, the CV technique was employed at a sweep rate of 50 mV/s with various concentrations of NF ranging from 50 to 350 μM (pH 7.0). The obtained CV signals are displayed in Figure 5A. Generally, the reaction zone between the $Pr_2Sn_2O_7$/GCE and the electrolyte is a two-dimensional surface, and the reaction taking place at the active $Pr_2Sn_2O_7$/GCE is an electrochemical−chemical−electrochemical (ECE) reaction. Obviously, with the successive addition of different concentrations, it is noted that the potentiodynamic reduction signal increases linearly in Figure 5A. Therefore, the concentration of the target species (NF) is directly coupled with the cathodic reduction current signal. Figure 5B shows the bar diagram for the different concentrations of NF versus cathodic reduction peak current, and it is derived from Figure 5A. Along with that, the linear regression equation with the correlation coefficient of I_{pc} (μA) = −0.050 [NF/μM] − 7.42; R^2 = 0.992 is obtained (Figure 5C). This clearly illustrates, from the electrochemical results obtained above, that the developed $Pr_2Sn_2O_7$ modified GCE feeds current with respect to NF concentration and it exhibits excellent conductivity toward NF sensing with its dominant active surface area, which mainly arises from the abundant oxygen vacancies in the lattice of pyrochlore oxide.

Influence of Scan Rate. The electrochemical kinetics behavior of the newly constructed $Pr_2Sn_2O_7$/GCE was investigated by using CV, in order to determine the number of electrons participating in the cathodic reduction of NF. It is customary to record the scan rate (υ) from 20 to 200 mV/s in an electrochemical cell containing 50 μM NF, and the acquired CV signals are shown in Figure 6A. From Figure 6B, it can be clearly observed that the cathodic current signal increases dramatically with respect to accelerating sweep rate in accordance with an excellent linear regression equation and correlation coefficient of I_{pc} (μA) = −0.028υ (mV/s) − 5.416; R^2 = 0.986. The number of electrons (n) was determined for NF reduction by exploiting the Bard and Faulkner analysis, and $E_p - E_{p/2}$ was determined to be 23.6 mV.[48] This value is consistent with an adsorption-controlled process for the reduction of NF at the $Pr_2Sn_2O_7$/GCE surface. The attained values was substituted in eq 3 to determine the n and α values.

$$E_p - E_{p/2} = (47.7/\alpha n)\ \text{mV} \tag{3}$$

where $E_{p/2}$ affirms the NF reduction peak potential. For the occurrence of the NF electrocatalytic reduction reaction, the involvement of electrons (n) was determined to be 4.01 and the charge transfer coefficient (α) was considered to be 0.55 for an irreversible process. Along with that, the reduction current shows a slight shift in a more negative direction with an increase in the sweep rate. The negative shift in the cathodic peak potential is in good agreement with the irreversible nature of the NF reduction reaction. Also, an outstanding linear dependent relationship is observed between the cathodic peak potential (E_{pc}) and ln υ (mV/s) with the linear regression equation and correlation coefficient of E_{pc} = −0.0156 ln υ (mV/s) − 0.394; R^2 = 0.993 (Figure 6C). Further, the standard heterogeneous rate constant (K_s) was calculated by acknowledging Laviron's model[47,48] for an irreversible electrochemical reaction using the given eq 4,

$$E_{pc} = E^\circ + (RT/\alpha nF)\ln(RTK_s/\alpha nF) + (RT/\alpha nF)\ln \upsilon \tag{4}$$

where E_{pc} corresponds to the cathodic peak potential, E° is the formal potential obtained from the intercept of E_{pc} plotted in

https://dx.doi.org/10.1021/acs.inorgchem.0c03377
Inorg. Chem. 2021, 60, 2464−2476

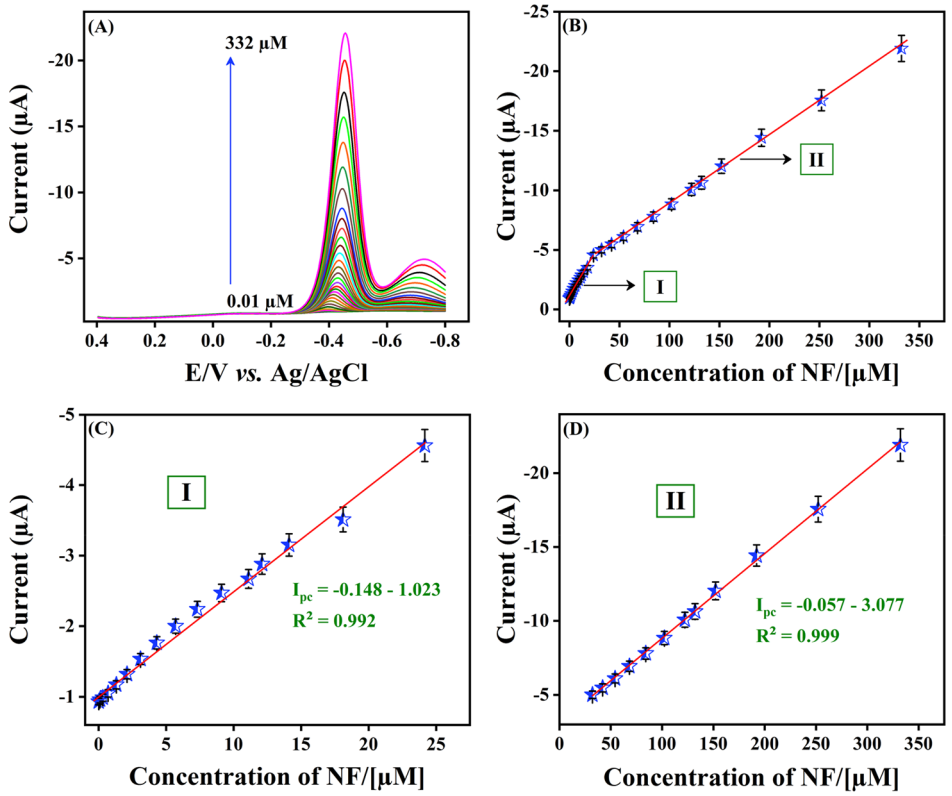

Figure 8. (A) DPV curves for successive additions of NF concentration from 0.01 to 332 μM in pH 7.0 with an amplitude of 0.05 V. (B) Calibration plot between the NF concentration vs cathodic signal. (C, D) Calibration plot for the lower (I) and higher (II) concentration ranges of NF obtained from panel (B).

accordance with ln υ (mV/s), R is the universal gas constant (8.314 J K^{-1} mol^{-1}), α is the electron transfer coefficient (0.55), T is the temperature (298 K), F is Faraday's constant (96485.3 C mol^{-1}), and n is the number of electrons. The standard heterogeneous rate constant (K_s) was calculated to be 6×10^{-3} cm^2 s^{-1}, and this illustrates the efficient interfacial charge transfer kinetic process at $Pr_2Sn_2O_7$/GCE affording the electrocatalytic reduction of NF.

Influence of pH. The NF electrocatalytic sensing and variation in the cathodic signal significantly depends on the choice of the pH of electrolyte solution (0.05 M PBS). Concerning this pH parameter, the NF cathodic reduction at $Pr_2Sn_2O_7$/GCE was tested by using CV at various pH values (pH 3.0−11.0) containing 50 μM NF under a N_2 saturated atmosphere at a scan rate of 50 mV/s. The achieved CV signals for pH studies are displayed in Figure 7A. It is clear that the reduction signal increases gradually from pH 3.0 to pH 7.0 and attains a maximal current intensity at pH 7.0 (Figure 7B). Subsequently, the reduction peak current decreases gradually when the pH is greater than 7.0. Followed by this, the cathodic peak potential also shifted to more a negative potential when increasing the pH from 3.0 to 7.0, suggesting the participation of protons (H^+) in the electrocatalytic NF reduction. Furthermore, the electrochemical activity of NF is completely pH-dependent and it will affect the sensing performance as well as the catalytic reaction rate of the electrode. From the above-obtained electrochemical findings, pH 7.0 was selected as an optimal electrolyte for pharmaceutical analysis and electrochemical investigations.

Calculation of Limit of Detection and Sensitivity. DPV is a more sensitive dynamic technique than CV; it was employed to obtain the amplification wave signals for LOD and sensitivity calculation of NF at $Pr_2Sn_2O_7$/GCE. The DPV test was carried out with a pulse width of 0.05 s and an amplitude of 0.05 V. Figure 8A shows that the cathodic amplification wave signal increases for each consecutive addition of NF on increasing the concentration from 0.01 to 332 μM.

A good linear relationship is obtained between the NF concentration and cathodic amplification pulse signals (Figure 8B). Along with that, the newly constructed electrode delivers two wide linear dynamic ranges from 0.01 to 24 μM (I, eq 5) and from 32 to 332 μM (II, eq 6). Figure 8C,D represents the calibration plots for the lower (I) and higher linear (II) ranges for cathodic signal vs NF concentration, and their corresponding linear regression equations with consistent correlation coefficients can be written as

$$I_{pc}(\mu A) = -0.148[NF/\mu M] - 1.023; \quad R^2 = 0.992 \qquad (5)$$

$$I_{pc}(\mu A) = -0.057[NF/\mu M] - 3.077; \quad R^2 = 0.999 \qquad (6)$$

Moreover, the designed $Pr_2Sn_2O_7$/GCE sensor exhibits an impressive LOD of 4 nM along with good sensitivity of 2.11 μA μM^{-1} cm^{-2}. The LOD and sensitivity were determined from the lower linear (I) calibration plot by using the equation of LOD = $3S_b/m$. From the DPV studies and results, it is clear that the designed sensor shows prominent electrocatalytic behavior with faster electron transfer mobility toward the sensitive detection of NF. The overall electrocatalytic performance of NF at $Pr_2Sn_2O_7$/GCE with a dynamic linear range and lower LOD is compared with the formerly reported NF sensors, as outlined in Table 1.

https://dx.doi.org/10.1021/acs.inorgchem.0c03377
Inorg. Chem. 2021, 60, 2464−2476

Table 1. Comparison of the NF Sensor with Different Modified Electrodes

working electrode	method	linear range (μM)	LOD (μM)	ref
Au-nanorod electrode-posited Au electrode	DPV	3.0−500	0.18	43
Au-nanorod electrode-posited Au electrode	amperometry	50−610	6.51	43
Ag_2WO_4/PPy/GCE modified electrode	DPV	0.1−107	0.012	44
double stranded DNA-modified GCE	DPV	2.5−37.5	0.8	49
static mercury drop electrode	cathodic stripping voltammetry	0.01−0.2	0.001	50
polyfurfural electrochemical RGO-GCE	DPV	1.0−50	0.25	46
high boron doped diamond	DPV	0.99−17	0.41	51
high boron doped diamond	DPV	0.99−11	0.34	51
carboxyl multiwalled carbon nanotubes/powder microelectrode	DPV	1−5000	645	52
carboxylic multiwalled carbon nanotubes/GCE reduction	amperometry	5−1090	224	53
$Pr_2Sn_2O_7$ NPs/GCE	DPV	0.01−24 (I) 32−332 (II)	0.004	this work

Selectivity, Repeatability, Reproducibility, and Storage Stability Studies. For endowing the selectivity of the newly developed $Pr_2Sn_2O_7$/GCE sensor, the selectivity was investigated by the DPV technique in pH 7.0 under N_2 atmosphere. Figure 9A displays the cathodic amplification wave impulses for the initial consecutive addition of 50 μM NF, followed by the sequential addition of the same concentration (50 μM) of biological molecules (uric acid, UA; ascorbic acid, AA), metal ions (Mg^{2+}, Ca^{2+}, Zn^{2+}, Ni^{2+}), and similar interfering nitro compounds (furazolidone, FZ; nitrofurantoin, NFT) in the same electrochemical cell. It can be seen that $Pr_2Sn_2O_7$/GCE exhibits a well-resolved NF reduction current signal at −0.41 V, while the addition of biological molecules and metal ions does not affect the NF peak current signal. However, the nitro compounds show a reduction wave next to the cathodic NF signal at −0.55 V, but this does not affect the NF signal. The obtained results clearly suggest that the fabricated $Pr_2Sn_2O_7$/GCE exhibits excellent selectivity for NF detection in the presence of different interfering compounds.

On the other hand, the reproducibility, repeatability, and storage stability of the constructed $Pr_2Sn_2O_7$/GCE were tested by using the DPV technique for 50 μM NF in pH 7.0. The obtained DPV curves are represented in Figure 9B−D. Figure 9B illustrates the repeatability of the peak current for the NF reduction at the electroactive surface of $Pr_2Sn_2O_7$/GCE for 10 consecutive repeated runs with the relative standard deviation (RSD) of 2.56%, indicating a well fabricated sensor with very good repeatability. Similarly, the reproducibility experiment of the fabricated sensor was carried out through four modified $Pr_2Sn_2O_7$/GCE by following the same construction protocol as mentioned earlier. Figure 9C shows excellent reproducibility with the RSD of 0.74%. Furthermore, the storage stability of the developed sensor was examined for 50 μM NF and the results are represented in Figure 9D. The electrochemical test was performed at a regular interval of 5 days for 2 weeks. In the meantime, $Pr_2Sn_2O_7$/GCE was carefully stored in a refrigerator at 4 °C. After 15 days, the fabricated $Pr_2Sn_2O_7$/GCE bears 97%

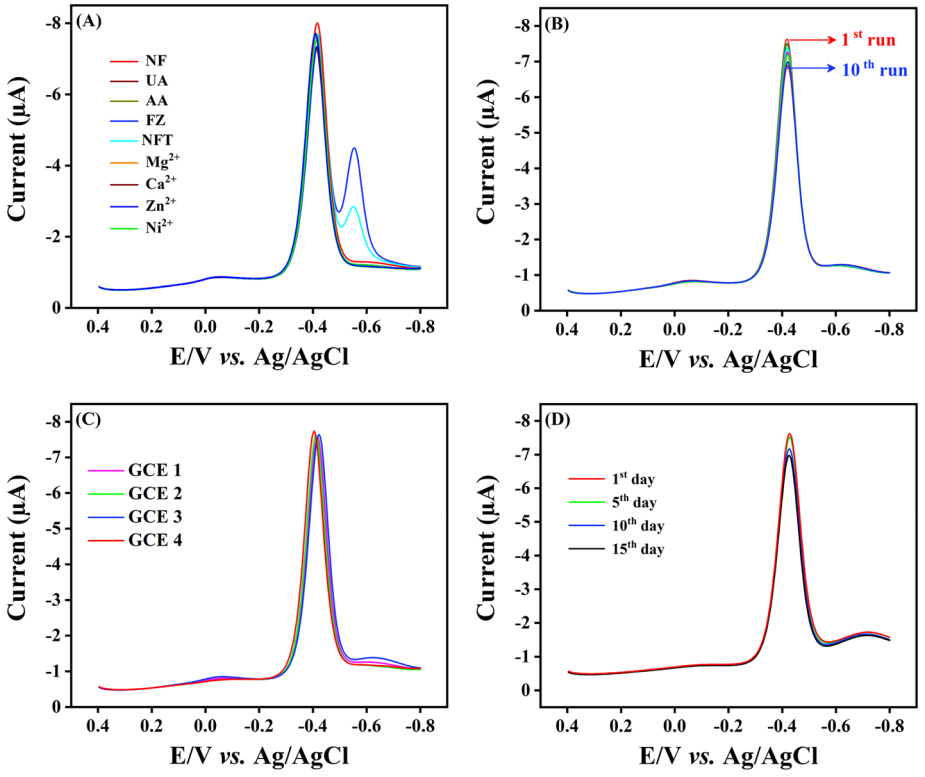

Figure 9. (A) Interference studies at $Pr_2Sn_2O_7$/GCE for 50 μM NF. (B) Repeatability, (C) reproducibility, and (D) storage stability studies for 50 μM NF at a sweep rate of 50 mV/s under N_2 atmosphere in pH 7.0.

https://dx.doi.org/10.1021/acs.inorgchem.0c03377
Inorg. Chem. 2021, 60, 2464−2476

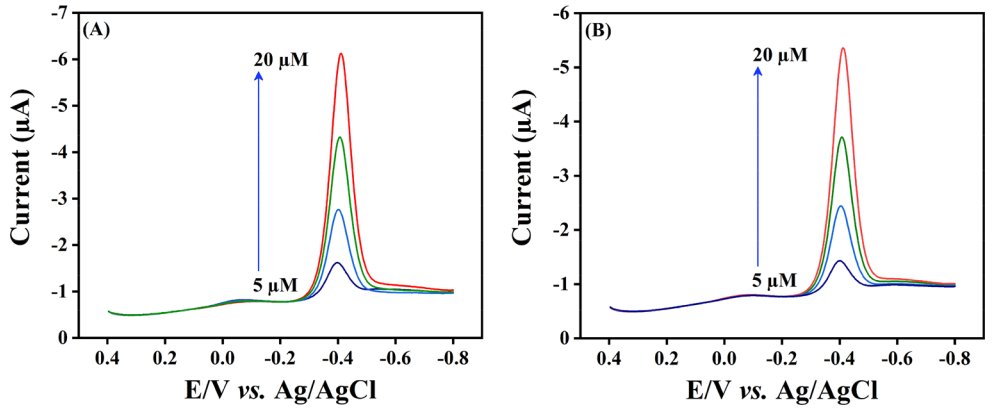

Figure 10. DPV amplification waves for the detection of NF in biological samples: (A) human serum and (B) human urine.

of its initial wave NF signal. These experimental results highlight the very good performance of the $Pr_2Sn_2O_7$/GCE sensor to achieve excellent repeatability, reproducibility, and storage stability toward affording the detection of NF.

Detection of NF in Human Blood Serum and Urine Samples. The fabricated $Pr_2Sn_2O_7$/GCE was used for the accurate detection of NF in biological samples (*i.e.*, human serum and urine samples) to assess the practical feasibility of the developed sensor. The real sample analysis studies were reviewed and approved by the ethics committee of Chang Gung Memorial Hospital (CGMH, Contract number. IRB No.201801660B and IRB99-3223C), Taiwan. The analysis was performed under the guidelines of the committee. Initially, the received human serum and urine samples were appropriately diluted to pH 7.0 and these samples were directly utilized for the analysis. However, these samples did not show any signal corresponding to the NF detection. Therefore, the known concentration of NF was spiked into the diluted solution and these solutions were used for the real sample analysis. The obtained DPV results for the detection of NF from 5 μM to 20 μM in human serum and urine samples are described in Figure 10. The NF injected values and recovery results were measured by using standard addition methods (Table 2). From Table 2, we achieved the higher recovery results between 94.8 and 99.73% (human blood serum sample), and 95.2 and 99.46% (urine sample) with RSD of less than 2%. Therefore, the developed $Pr_2Sn_2O_7$/GCE sensor exhibits acceptable recovery results and it evidently proves that the designed sensor affirms its potential in real-time pharmaceutical and biological applications.

Table 2. Electroanalytical Detection of NF in Biological Samples

sample	added (μM)	found (μM)	recovery (%)
human blood serum	0		
	5	4.94	98.8
	10	9.48	94.8
	15	14.96	99.73
	20	19.59	97.95
human urine	0		
	5	4.76	95.2
	10	9.85	98.5
	15	14.92	99.46
	20	19.54	97.7

CONCLUSION

For the first time, we have synthesized high crystalline RE-pyrochlore $Pr_2Sn_2O_7$ NPs by using a facile coprecipitation synthesis method followed by calcination. The fabricated $Pr_2Sn_2O_7$ NPs modified GCE was employed as a novel electrocatalyst toward the electrochemical detection of the antibiotic drug NF. In addition, various analytical and spectroscopic techniques such as XRD, FE-SEM, HR-TEM, Raman, and XPS analysis were used to characterize the prepared $Pr_2Sn_2O_7$ NPs, while the detection of NF was achieved with different voltammetry techniques. From the analysis, we have reported an ultralow detection limit (4 nM), high sensitivity (2.11 $\mu A\ \mu M^{-1}\ cm^{-2}$), and excellent selectivity in the presence of a similar structure containing drugs, biomolecules, and metal ions for the electrochemical reduction of NF. The as-prepared pyrochlore oxide $Pr_2Sn_2O_7$ NPs serve as a potential and promising electrode active material for the detection of NF in real-time pharmaceutical and biological applications.

ASSOCIATED CONTENT

Supporting Information

The Supporting Information is available free of charge at https://pubs.acs.org/doi/10.1021/acs.inorgchem.0c03377.

Cyclic voltammograms loading results and elemental mapping images of $Pr_2Sn_2O_7$ NPs (PDF)

AUTHOR INFORMATION

Corresponding Authors

Shen Ming Chen − *Electroanalysis and Bioelectrochemistry Lab, Department of Chemical Engineering and Biotechnology, National Taipei University of Technology, Taipei 106, Taiwan, ROC*; orcid.org/0000-0002-0132-9161; Phone: +886-2270-17147; Email: smchen78@ms15.hinet.net; Fax: +886-2270-25238

P. Muhammed Shafi − *School of Chemical Engineering, Yeungnam Universit, Gyeongsan, Gyeongbuk 38541, Republic of Korea*; Phone: +82-5138-1125; Email: shafiparasseri@gmail.com

Authors

Ramachandran Rajakumaran − *Electroanalysis and Bioelectrochemistry Lab, Department of Chemical Engineering and Biotechnology, National Taipei University of Technology, Taipei 106, Taiwan, ROC*

Ramaraj Sukanya − *Electroanalysis and Bioelectrochemistry Lab, Department of Chemical Engineering and Biotechnology,*

https://dx.doi.org/10.1021/acs.inorgchem.0c03377
Inorg. Chem. 2021, 60, 2464−2476

National Taipei University of Technology, Taipei 106, Taiwan, ROC

Raj Karthik − *School of Chemical Engineering, Yeungnam Universit, Gyeongsan, Gyeongbuk 38541, Republic of Korea;* orcid.org/0000-0002-8605-643X

Carmel B. Breslin − *Department of Chemistry, Maynooth University, Maynooth, Co. Kildare W23 FH6, Ireland;* orcid.org/0000-0002-0586-5375

Complete contact information is available at: https://pubs.acs.org/10.1021/acs.inorgchem.0c03377

Notes

The authors declare no competing financial interest.

■ ACKNOWLEDGMENTS

The authors acknowledge the Ministry of Science and Technology (MOST 107-2113-M-027-005-MY3), Taiwan.

■ REFERENCES

(1) Bian, J.; Li, Z.; Li, N.; Sun, C. Oxygen Deficient $LaMn_{0.75}Co_{0.25}O_{3-3}$ Nanofibers as an Efficient Electrocatalyst for Oxygen Evolution Reaction and Zinc-Air Batteries. *Inorg. Chem.* **2019**, *58* (12), 8208−8214.

(2) Bian, J.; Su, R.; Yao, Y.; Wang, J.; Zhou, J.; Li, F.; Wang, Z. L.; Sun, C. Mg Doped Perovskite $LaNiO_3$ Nanofibers as an Efficient Bifunctional Catalyst for Rechargeable Zinc-Air Batteries. *ACS Appl. Energy Mater.* **2019**, *2* (1), 923−931.

(3) Sun, C.; Stimming, U. Recent Anode Advances in Solid Oxide Fuel Cells. *J. Power Sources* **2007**, *171* (2), 247−260.

(4) Sun, C.; Alonso, J. A.; Bian, J. Recent Advances in Perovskite-Type Oxides for Energy Conversion and Storage Applications. *Adv. Energy Mater.* **2021**, *11*, 2000459.

(5) Feng, Q.; Zhang, Z.; Huang, H.; Yao, K.; Fan, J.; Zeng, L.; Williams, M. C.; Li, H.; Wang, H. An Effective Strategy to Tune the Oxygen Vacancy of Pyrochlore Oxides for Electrochemical Energy Storage and Conversion Systems. *Chem. Eng. J.* **2020**, *395*, 124428.

(6) Kim, M.; Ju, H.; Kim, J. Single Crystalline $Bi_2Ru_2O_7$ Pyrochlore Oxide Nanoparticles as Efficient Bifunctional Oxygen Electrocatalyst for Hybrid Na-Air Batteries. *Chem. Eng. J.* **2019**, *358*, 11−19.

(7) Abbott, D. F.; Pittkowski, R. K.; MacOunová, K.; Nebel, R.; Marelli, E.; Fabbri, E.; Castelli, I. E.; Krtil, P.; Schmidt, T. J. Design and Synthesis of Ir/Ru Pyrochlore Catalysts for the Oxygen Evolution Reaction Based on Their Bulk Thermodynamic Properties. *ACS Appl. Mater. Interfaces* **2019**, *11* (41), 37748−37760.

(8) Park, J.; Risch, M.; Nam, G.; Park, M.; Shin, T. J.; Park, S.; Kim, M. G.; Shao-Horn, Y.; Cho, J. Single Crystalline Pyrochlore Nanoparticles with Metallic Conduction as Efficient Bi-Functional Oxygen Electrocatalysts for Zn-Air Batteries. *Energy Environ. Sci.* **2017**, *10* (1), 129−136.

(9) Kim, M.; Park, J.; Kang, M.; Kim, J. Y.; Lee, S. W. Toward Efficient Electrocatalytic Oxygen Evolution: Emerging Opportunities with Metallic Pyrochlore Oxides for Electrocatalysts and Conductive Supports. *ACS Cent. Sci.* **2020**, *6* (6), 880−891.

(10) Suntivich, J.; Gasteiger, H. A.; Yabuuchi, N.; Nakanishi, H.; Goodenough, J. B.; Shao-Horn, Y. Design Principles for Oxygen-Reduction Activity on Perovskite Oxide Catalysts for Fuel Cells and Metal-Air Batteries. *Nat. Chem.* **2011**, *3*, 546−550.

(11) Ewing, R. C.; Weber, W. J.; Lian, J. Nuclear Waste Disposal-Pyrochlore ($A_2B_2O_7$): Nuclear Waste Form for the Immobilization of Plutonium and "Minor" Actinides. *J. Appl. Phys.* **2004**, *95*, 5949−5971.

(12) Cao, X. Q.; Vassen, R.; Stoever, D. Ceramic Materials for Thermal Barrier Coatings. *J. Eur. Ceram. Soc.* **2004**, *24* (1), 1−10.

(13) Winter, M. R.; Clarke, D. R. Oxide Materials with Low Thermal Conductivity. *J. Am. Ceram. Soc.* **2007**, *90* (2), 533−540.

(14) Gardner, J. S.; Gingras, M. J. P.; Greedan, J. E. Magnetic Pyrochlore Oxides. *Rev. Mod. Phys.* **2010**, *82* (1), 53−107.

(15) Martin, N.; Bonville, P.; Lhotel, E.; Guitteny, S.; Wildes, A.; Decorse, C.; Hatnean, M. C.; Balakrishnan, G.; Mirebeau, I.; Petit, S. Disorder and Quantum Spin Ice. *Phys. Rev. X* **2017**, *7* (4), 041028.

(16) Bonville, P.; Guitteny, S.; Gukasov, A.; Mirebeau, I.; Petit, S.; Decorse, C.; Hatnean, M. C.; Balakrishnan, G. Magnetic Properties and Crystal Field in $Pr_2Zr_2O_7$. *Phys. Rev. B: Condens. Matter Mater. Phys.* **2016**, *94* (13), 134428.

(17) Yamamura, H.; Nishino, H.; Kakinuma, K.; Nomura, K. Electrical Conductivity Anomaly around Fluorite-Pyrochlore Phase Boundary. *Solid State Ionics* **2003**, *158*, 359−365.

(18) Brik, M. G.; Srivastava, A. M.; Ma, C. G.; Piasecki, M. Dependence of the Mn^{4+} Spectroscopic Properties on the Host Composition: Case Study of Stannate Pyrochlores $A_2Sn_2O_7$ (A = La, Gd, Y, Lu). *J. Lumin.* **2020**, *218*, 116834.

(19) Munawar, K.; Mansoor, M. A.; Olmstead, M. M.; Yusof, F. B.; Misran Bin, M.; Basirun, W. J.; Mazhar, M. Pyrochlore-Structured $Y_2Ti_2O_7$-$2TiO_2$ Composite Thin Films for Photovoltaic Applications. *J. Aust. Ceram. Soc.* **2019**, *55* (4), 921−932.

(20) Petrov, V. G.; Chen, Z.; Romanchuk, A. Y.; Demina, V. O.; Tang, Y.; Kalmykov, S. N. Sorption of Eu (III) onto Nano-Sized H-Titanates of Different Structures. *Appl. Sci.* **2019**, *9* (4), 697.

(21) Feng, Q.; Zhao, Z.; Yuan, X. Z.; Li, H.; Wang, H. Oxygen Vacancy Engineering of Yttrium Ruthenate Pyrochlores as an Efficient Oxygen Catalyst for Both Proton Exchange Membrane Water Electrolyzers and Rechargeable Zinc-Air Batteries. *Appl. Catal., B* **2020**, *260* (2019), 118176.

(22) Zinatloo-Ajabshir, S.; Morassaei, M. S.; Amiri, O.; Salavati-Niasari, M.; Foong, L. K. $Nd_2Sn_2O_7$ Nanostructures: Green Synthesis and Characterization Using Date Palm Extract, a Potential Electrochemical Hydrogen Storage Material. *Ceram. Int.* **2020**, *46* (11), 17186−17196.

(23) Prabhakaran, D.; Wang, S.; Boothroyd, A. T. Crystal Growth of Pyrochlore Rare-Earth Stannates. *J. Cryst. Growth* **2017**, *468*, 335−339.

(24) Kaliyaperumal, C.; Jayabalan, S.; Sankarakumar, A.; Paramasivam, T. Structural and Electrical Characteristics of Nanocrystalline $La_2Sn_2O_7$ Pyrochlore. *Solid State Sci.* **2020**, *105*, 106245.

(25) Zinatloo-Ajabshir, S.; Morassaei, M. S.; Amiri, O.; Salavati-Niasari, M. Green Synthesis of Dysprosium Stannate Nanoparticles Using Ficus Carica Extract as Photocatalyst for the Degradation of Organic Pollutants under Visible Irradiation. *Ceram. Int.* **2020**, *46* (5), 6095−6107.

(26) Abraham, A.; Gupta, S. K.; Mohan, S.; Abdou, H.; Mao, Y. Defect-Induced Optical and Electrochemical Properties of $Pr_2Sn_2O_7$ Nanoparticles Enhanced by Bi^{3+} Doping. *J. Mater. Res.* **2020**, *35* (9), 1214−1224.

(27) Cheng, J.; Li, Y.; Zhong, J.; Lu, Z.; Wang, G.; Sun, M.; Jiang, Y.; Zou, P.; Wang, X.; Zhao, Q. Molecularly Imprinted Electrochemical Sensor Based on Biomass Carbon Decorated with MOF-Derived Cr_2O_3 and Silver Nanoparticles for Selective and Sensitive Detection of Nitrofurazone. *Chem. Eng. J.* **2020**, *398*, 125664.

(28) Gupta, V. K.; Jain, R.; Radhapyari, K.; Jadon, N.; Agarwal, S. Voltammetric Techniques for the Assay of Pharmaceuticals-A Review. *Anal. Biochem.* **2011**, *408* (2), 179−196.

(29) Gupta, A.; Upadhyay, N. K.; Parthasarathy, S.; Rajagopal, C.; Roy, P. K. Nitrofurazone-Loaded PVA-PEG Semi-IPN for Application as Hydrogel Dressing for Normal and Burn Wounds. *J. Appl. Polym. Sci.* **2013**, *128* (6), 4031−4039.

(30) Bot, C.; Hall, B. S.; Álvarez, G.; Di Maio, R.; González, M.; Cerecetto, H.; Wilkinson, S. R. Evaluating 5-Nitrofurans as Trypanocidal Agents. *Antimicrob. Agents Chemother.* **2013**, *57* (4), 1638−1647.

(31) Khong, S. P.; Gremaud, E.; Richoz, J.; Delatour, T.; Guy, P. A.; Stadler, R. H.; Mottier, P. Analysis of Matrix-Bound Nitrofuran Residues in Worldwide-Originated Honeys by Isotope Dilution High-Performance Liquid Chromatography-Tandem Mass Spectrometry. *J. Agric. Food Chem.* **2004**, *52* (17), 5309−5315.

(32) Hiraku, Y.; Sekine, A.; Nabeshi, H.; Midorikawa, K.; Murata, M.; Kumagai, Y.; Kawanishi, S. Mechanism of Carcinogenesis Induced by a

Veterinary Antimicrobial Drug, Nitrofurazone, via Oxidative DNA Damage and Cell Proliferation. *Cancer Lett.* **2004**, *215* (2), 141−150.
(33) Pearson, R. A.; Evans, C.; Bendall, J. G. Nitrofurazone Quantification in Milk at the European Union Minimum Required Performance Limit of 1 ng g^{-1}: Circumventing the Semicarbazide Problem. *Food Addit. Contam., Part A* **2016**, *33* (8), 1324−1336.
(34) Shahjahan, M.; Shalaby, A. Determination of Nitrofurazone in Some Pharmaceutical Preparations. *Int. J. Pharm.* **1998**, *168* (2), 169−172.
(35) Tubino, M.; Vila, M. M. D. C.; Palumbo, M. N. Determination of Nitrofurazone in Topical Pharmaceutical Preparations: Comparison of the UV-Visible Diffuse Reflectance versus Transmittance versus HPLC Methods. *J. Braz. Chem. Soc.* **2009**, *20* (10), 1901−1907.
(36) Sreena, T. S.; Prabhakar Rao, P.; Raj, A. K. V.; Aju Thara, T. R. Exploitation of Eu^{3+} Red Luminescence through Order-Disorder Structural Transitions in Lanthanide Stannate Pyrochlores for Warm White LED Applications. *Phys. Chem. Chem. Phys.* **2018**, *20* (37), 24287−24299.
(37) Teixeira, A. R. F. A.; de Meireles Neris, A.; Longo, E.; de Carvalho Filho, J. R.; Hakki, A.; Macphee, D.; dos Santos, I. M. G. $SrSnO_3$ Perovskite Obtained by the Modified Pechini Method—Insights about Its Photocatalytic Activity. *J. Photochem. Photobiol., A* **2019**, *369*, 181−188.
(38) Zhang, T. T.; Li, K. W.; Zeng, J.; Wang, Y. L.; Song, X. M.; Wang, H. Synthesis and Structural Characterization of a Series of Lanthanide Stannate Pyrochlores. *J. Phys. Chem. Solids* **2008**, *69* (11), 2845−2851.
(39) Denisova, L. T.; Kargin, Y. F.; Denisov, V. M. Heat Capacity of Rare-Earth Stannates in the Range 350−1000 K. *Inorg. Mater.* **2017**, *53* (9), 956−961.
(40) Gnanamoorthy, G.; Ramar, K.; Padmanaban, A.; Yadav, V. K.; Suresh Babu, K.; Karthikeyan, V.; Narayanan, V. Implementation of $ZnSnO_3$ Nanosheets and Their RE (Er, Eu, and Pr) Materials: Enhanced Photocatalytic Activity. *Adv. Powder Technol.* **2020**, *31* (3), 1209−1219.
(41) Yamuna, A.; Sundaresan, P.; Chen, S. M.; Shih, W. L. Ultrasound Assisted Synthesis of Praseodymium Tungstate Nanoparticles for the Electrochemical Detection of Cardioselective *β*-Blocker Drug. *Microchem. J.* **2020**, *159*, 105420.
(42) Muthukutty, B.; Krishnapandi, A.; Chen, S. M.; Abinaya, M.; Elangovan, A. Innovation of Novel Stone-Like Perovskite Structured Calcium Stannate ($CaSnO_3$): Synthesis, Characterization, and Application Headed for Sensing Photographic Developing Agent Metol. *ACS Sustainable Chem. Eng.* **2020**, *8* (11), 4419−4430.
(43) Rahi, A.; Sattarahmady, N.; Dehdari Vais, R.; Heli, H. Sonoelectrodeposition of Gold Nanorods at a Gold Surface - Application for Electrocatalytic Reduction and Determination of Nitrofurazone. *Sens. Actuators, B* **2015**, *210*, 96−102.
(44) Manickavasagan, A.; Ramachandran, R.; Chen, S. M.; Velluchamy, M. Ultrasonic Assisted Fabrication of Silver Tungstate Encrusted Polypyrrole Nanocomposite for Effective Photocatalytic and Electrocatalytic Applications. *Ultrason. Sonochem.* **2020**, *64*, 104913.
(45) De Lima Brito, C.; Trossini, G. H. G.; Ferreira, E. I.; La-Scalea, M. A. Nitrofurazone and Its Nitroheterocyclic Analogues: A Study of the Electrochemical Behavior in Aqueous Medium. *J. Braz. Chem. Soc.* **2013**, *24* (12), 1964−1973.
(46) Ye, F.; Huang, J.; Xu, Y.; Zeng, Q.; Nan, J.; Wang, L. Polyfurfural-Electrochemically Reduced Graphene Oxide Modified Glassy Carbon Electrode for the Direct Determination of Nitrofurazone; *Anal. Lett.* **2018**, *51* (5), 728−741.
(47) Brahman, P. K.; Suresh, L.; Reddy, K. R.; Bondili, J. S. An Electrochemical Sensing Platform for Trace Recognition and Detection of an Anti-Prostate Cancer Drug Flutamide in Biological Samples. *RSC Adv.* **2017**, *7* (60), 37898−37907.
(48) Karuppaiah, B.; Ramachandran, R.; Chen, S. M.; Wan-Ling, S.; Wan, J. Y. Hierarchical Construction and Characterization of Lanthanum Molybdate Nanospheres as an Unassailable Electrode Material for Electrocatalytic Sensing of the Antibiotic Drug Nitrofurantoin. *New J. Chem.* **2020**, *44* (1), 46−54.
(49) Ni, Y.; Wang, P.; Kokot, S. Voltammetric Investigation of DNA Damage Induced by Nitrofurazone and Short-Lived Nitro-Radicals with the Use of an Electrochemical DNA Biosensor. *Biosens. Bioelectron.* **2012**, *38* (1), 245−251.
(50) Khodari, M.; Mansour, H.; A.M. Mersal, G. Cathodic Stripping Voltammetric Behaviour of Nitrofurazone and Its Determination in Pharmaceutical Dosage Form, Urine and Serum by Linear Sweep Voltammetry. *J. Pharm. Biomed. Anal.* **1999**, *20* (3), 579−586.
(51) Julião, M. S. d. S.; Ferreira, E. I.; Ferreira, N. G.; Serrano, S. H. P. Voltammetric Detection of the Interactions between RNO_2\{radical Dot\}- and Electron Acceptors in Aqueous Medium at Highly Boron Doped Diamond Electrode (HBDDE). *Electrochim. Acta* **2006**, *51* (24), 5080−5086.
(52) He, B. S.; Dong, X. Z. Powder Microelectrode Embedded with Carboxyl Multi-Walled Carbon Nanotubes for Sensitive and Quantitative Detection of Nitrofuran Residues. *Anal. Methods* **2018**, *10* (11), 1372−1378.
(53) He, B.; Li, M. Rapid Detection of Nitrofuran and Its Metabolites by Using Carboxylic Multi-Walled Carbon Nanotubes Modified Glassy Carbon Electrode. *Int. J. Electrochem. Sci.* **2018**, *13* (5), 4171−4181.

https://dx.doi.org/10.1021/acs.inorgchem.0c03377
Inorg. Chem. 2021, 60, 2464−2476